Available online at www.sciencedirect.com
SCIENCE DIRECT®
ELSEVIER
International Journal of Solids and Structures 41 (2004) 6677–6697
INTERNATIONAL JOURNAL OF SOLIDS and STRUCTURES
www.elsevier.com/locate/ijsolstr

On the strength enhancement under impact loading of square tubes made from rate insensitive metals

Han Zhao *, Salim Abdennadher

Laboratoire de Mécanique et Technologie-Cachan, ENS-Cachan/CNRS/Université Pierre & Marie Curie (Paris 6), 61 Avenue du président Wilson, 94235 Cachan cedex, France

Received 16 May 2004
Available online 17 July 2004

Abstract

This paper presents a study on the strength enhancement of a model structure (square tubes) under impact loading. It aims at the understanding of the impact strength enhancement in a successive folding process of some cellular structures (aluminium powder metallurgy foams and honeycombs).

Compressive crushing tests of square tubes made of brass were performed under static and dynamic loading. A significant enhancement (up to 40%) of peak loads was found in successive folding cycles. Static and dynamic compressive tests on specimens cut from these brass tubes were also performed to prove the rate insensitivity of the brass itself, demonstrating the increase of the crush resistance of the brass square tube in successive folding is not caused by the rate sensitivity of the base material.

Numerical simulations of crushing tests under static and impact loading were performed to obtain local information such as the time histories of stress and strain fields everywhere in the tube, which are difficult to measure under impact loading. The simulations indicated that the regions around the four edges of a square tube remain straight even when the flat plates between two adjacent edges are already strongly bent. Furthermore, the straight edge line zones support about 80% of the global crushing load. Therefore, buckling of these edge-areas determines the peak loads in successive folding cycles.

Theoretical analysis of an idealized square box column model leads to a reasonable prediction of successive crushing peak loads in both static and dynamic cases. Under impact loading, the strain reached in these edge-areas is higher because of inertia. Strain hardening of the base material is the reason for the increase of crushing forces. Post-mortem micro-hardness measurements confirmed this theory and a good agreement between experiment and simulation was found.

Keywords: Strain rate; Tube; Impact; Inertia; Micro-buckling; Honeycombs; Foam

* Corresponding author. Tel.: +33-1-47402039; fax: +33-1-47402240.
E-mail address: zhao@lmt.ens-cachan.fr (H. Zhao).

0020-7683/$ - see front matter © 2004 Elsevier Ltd. All rights reserved.
doi:10.1016/j.ijsolstr.2004.05.039

1. Introduction

Cellular materials such as aluminium foams, agglomerates of nickel hollow spheres, honeycombs and assemblies of beams may lead to a technological revolution in the domain of lightweight designs (Banhart, 2001). A great number of experimental, numerical, and analytical studies have been reported in the open literature (Wierzbicki, 1983; Gibson and Ashby, 1988; Klintworth and Stronge, 1988; Reid and Peng, 1997; Deshpande and Fleck, 2000a; Hanssen et al., 2002).

The behaviour of cellular materials under dynamic loading is an important goal because one of the main applications of cellular materials is to absorb energy in accidental impacts. In the case of metallic foams, Deshpande and Fleck (2000b) reported dispersed results and suggested no rate sensitivity. However, other works (Mukai et al., 1999; Tan et al., 2002; Zhao, 2004) show a significant rate sensitivity. For aluminium honeycombs, the rate sensitivity has been studied more. Goldsmith and Sackman (1992) reported experimental work on out-of-plane crushing. They fired a rigid projectile at a target made of honeycombs and showed that the mean crushing pressures were sometimes up to 50% higher than the static results. Wu and Jiang (1997) also studied out-of-plane crushing with a similar experimental technique and reported a significant enhancement of the crushing strength. Using a nylon SHPB, Zhao and Gary (1998) confirmed these results.

The observed strength enhancement can neither be explained by the behaviour at high strain rates of the base-materials nor by the air trapped in the cells (Deshpande and Fleck, 2000b). It should be also noted that this strength enhancement of cellular materials was observed in the range of moderate impact velocities (<50 m/s). Therefore, the model of shock enhancement reported by Reid and Peng (1997) does not apply.

For this strength enhancement under moderate impact velocities, another possible factor is inertia. The early theoretical work in this domain was reported by Budiansky and Hutchinson (1964). It has been experimentally shown that the buckling of a column under compressive impact occurs at a larger strain because of lateral inertia, so that the critical buckling force is higher than in the static case (Gary, 1983). Other published work (Calladine and English, 1984; Tam and Calladine, 1991) explained in detail the role played by lateral inertia. These authors studied experimentally the buckling and post-buckling behaviour of a simple column under impact loading and developed simple models.

To outline the basic idea without mathematical details, let us consider a simple model made of two massless rigid plastic bars linked by a plastic hinge with a concentrated mass in the middle as an example (Fig. 1).

This mechanical system is well defined. The following geometrical relationship holds:

$$\delta v = -L \sin\theta \delta\theta \tag{1}$$

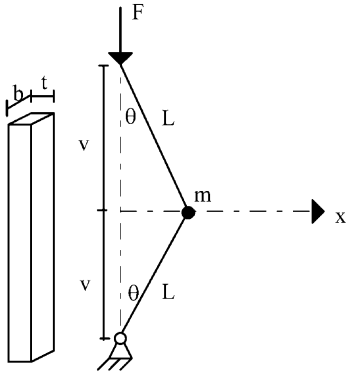

Fig. 1. Simple rigid plastic bars model.

Under static loading, the system will collapse (the angle θ will increase rapidly) once the maximum moment due to the applied force F overcomes the fully plastic moment of the plastic hinge $M_p = bt^2\sigma_s/4$.

$$F = M_p\left|\frac{2\delta\theta}{2\delta v}\right| = \frac{\sigma_s bt^2}{4L\sin\theta} \tag{2}$$

The initial imperfection (deviation from a vertically straight position) is characterized by the angle θ. If the angle is zero, there will be no buckling but only compression. For a reasonably small angle, the buckling peak load is almost equal to the product of the flow stress with the cross-sectional area.

When the model is loaded with sudden imposed higher speeds, the same peak load as in the static case is reached instantly. However, the collapse of the system depends still on the motion of the concentrated mass in the middle. Indeed, the lateral acceleration of this concentrated mass is governed by the force transmitted to it by the bars.

$$m\ddot{x} = 2N\sin\theta \tag{3a}$$

As the force transmitted by the bars is limited by their plastic flow stress, the acceleration of the mass has a maximum value given by:

$$m\ddot{x} \leqslant 2\sigma_s bt\sin\theta \tag{3b}$$

Initially, the concentrated mass is at rest and its acceleration is limited to the value given by the inequality (3b). It takes time to reach the speed kinematically compatible with the loading impact velocity. During this acceleration period, the global crushing displacement is mostly given by the compression of bars. The rotation is very small because the mass cannot move rapidly. The compressive strain reached before collapse under impact loading is therefore higher than in the static case. If moreover, the column is made of strain hardening material, the buckling force will be higher because the buckling strain in the column is higher under impact loading. It should be noted that initial imperfections play a very important role here: the smaller the initial imperfection, the stronger is this inertia effect.

Such a basic concept was used by a number of authors to explain the observed strength increase under impact. Su et al. (1995) gave a classification of different structures as to whether they are rate sensitive or not. Langseth and Hopperstad (1996), Langseth et al. (1999) considered that lateral inertia is a cause of the strength increase observed in steel and aluminium square tubes. The wavelength of successive folding can be modified by stress wave propagation (Karagiozova et al., 2000) which leads to the strength enhancement. In the case of crushing of fibre composites, inertia prevents the composites from kicking and so splitting takes place under impact loading. This leads to a higher crushing force (Oguni and Ravichandran, 2000, 2001). In the case of cellular materials, it was observed for Balsa wood that the folding wavelength becomes smaller (Vural and Ravichandran, 2003) under impact loading, explaining its higher crushing strength under impact.

For some cellular materials, such as Powder metallurgy IFAM Al6061 (left part of Fig. 2) or Al5056 honeycombs (middle part of Fig. 2), a significant strength enhancement is observed. The crushing mode is successive folding of cell walls. However, no noticeable wavelength change was found (Abdennadher, 2004). The known mechanisms described above do not give a clear explanation. In order to determine the factor responsible for strength enhancement under impact in a successive folding process, we studied a model-structure: commercially available brass square tube (after suitable partial annealing). The observed crushing mode of such tubes (right part of Fig. 2) is also successive folding of walls. In addition, the behaviour of brass is known to be rate insensitive for a large range of strain rates.

Our experimental studies of brass square tubes are presented to confirm that strength enhancement under impact can occur without changes in the folding wavelength. The annealing and quenching process of the brass tubes is described. The aim was to obtain repeatable material characteristics and also a suitable

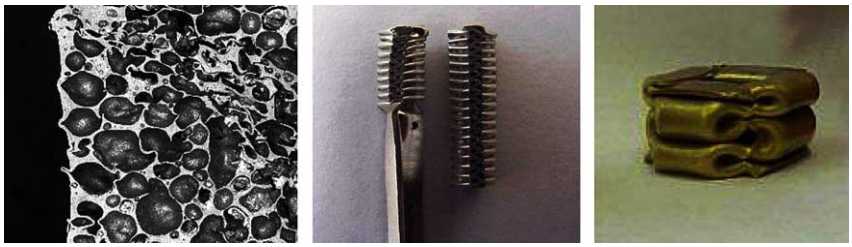

Fig. 2. Crushing by ductile successive folding.

successive folding mode. Material characterization tests under static and dynamic loading up to 2500/s were performed to ensure that there is no rate sensitivity for brass in this range of strain rates.

Numerical simulations of these static and dynamic tests were performed, which yielded quite accurate correlations between experimental and numerical geometrical profiles during crushing as well as force–displacement curves. Such numerically simulated tests provide local information such as stress and strain histories everywhere, which are impossible to measure experimentally, especially under impact. This local information shows that load enhancement is due to lateral inertia because the regions around the four corners remain vertically straight during the early stage of the folding cycle. An idealized simple square box column model is presented to describe how the inertia effect works in a square tube.

Lastly, post-mortem micro-hardness measurement were performed on tubes that had subjected to both static and dynamic loading to various degree of crushing in order to validate the whole theory. The hardness can be related to the local plastic strain, with the help of reference tests giving an experimental strain–hardness relationship. Good agreement between micro-hardness measurements and simulations provided a validation test.

2. Experimental study of the crushing strength of brass square tubes

35 mm × 35 mm commercial brass square tubes of 1.5 mm wall thickness were chosen because of the restrictions of the testing device. However, strain hardening produced during manufacturing made the as-received tubes brittle so that the successive crushing mode was not observed because of early fractures at the four edges. Annealing was therefore necessary in order to make the tubes more ductile. To obtain a repeatable heat treatment, the exact chemical composition of the brass tubes (Cu 64%, Zn 36%) were measured using an EDS microprobe. The corresponding phase equilibrium diagram indicates the temperature range needed. The following heat treatment was performed: 30 min annealing at 450 °C and water quenching.

2.1. Experimental characterization of the rate sensitivity of brass

Tests under a comparable loading mode (static as well as dynamic) were performed to determine if the partially annealed base material (brass) is rate insensitive. Compressive tests were chosen for the following reasons: (i) the main loading mode in tube crushing is compression; (ii) under dynamic loading, compression with an SHPB (Split Hopkinson pressure bar) is much more accurate than tension because of the specimen shape and attachment difficulties.

Specimens were cut from heat-treated brass tubes. Their dimensions were about 1.5 mm thick, 2 mm high and 10 mm wide. Such specimens were tested with an MTS810 universal testing machine at 0.001 mm/s. The force was measured by the load cell of the machine. As the specimen height was small (2 mm), it is

hard to attach a strain gage or an extensometer to the specimen. The displacement measurement of the machine is believed not to be accurate enough to obtain a reliable strain measurement, even if the stiffness of the test machine is known and corrected for. An alternative is to use an optical displacement field measurement. The principle is to compare images of the specimen taken during the test by means of a Kodak Megaplus CCD camera and a long-distance microscope Questar QM100. An image processing technique based on cross-correlation allows matching of the same material points in different images, thus giving their displacements. The software developed at our laboratory (Laboratoire de Mécanique et Technologie) was used to perform this image processing task. It can give sub-pixel accuracy for displacement and a precision in the strain of at least 10^{-4} with an 8-bit 1008×1016 pixel optical camera (Hild et al., 1999; Chevalier et al., 2001). Such optical measurement of the strain field provides a check on the effect of friction as well as the parallelism of the two faces. It proved that the test produces a uniform compression.

Dynamic tests were performed with a Split Hopkinson Pressure Bar or Kolsky apparatus (Hopkinson, 1914; Kolsky, 1949). A steel SHPB of 20 mm diameter was used. The specimen was placed between two bars. It was also lubricated to reduce friction. Signals were sampled at 1 MHz using an integrated data acquisition card. One problem in the use of the SHPB is the application of the correct shift to the elastic waves measured at the midpoints of the bars to the bar-specimen interfaces where the forces and velocities are needed. Careful data processing is necessary to obtain this shift (Davies, 1948; Zhao and Gary, 1995, 1996), which was performed with the special program DAVID written at the Laboratoire de Mécanique des Solides. The classical analysis, which assumes the axial uniformity of the stress and strain fields in the specimen, was used (Zhao and Gary, 1996). The experimental results were reproducible with nearly no scatter. Fig. 3 shows a comparison of the stress/strain response of annealed brass from quasi-static up to strain rates of 2500/s. There is no observable rate sensitivity.

2.2. Strength enhancement of brass square tubes

Static crushing tests were performed on heat-treated tubes with a universal testing machine. To avoid a global elastic buckling mode, the length of the tube specimen was chosen as 104 mm. The successive folding mode was observed. The load cell and displacement measurement of the test machine were used to record

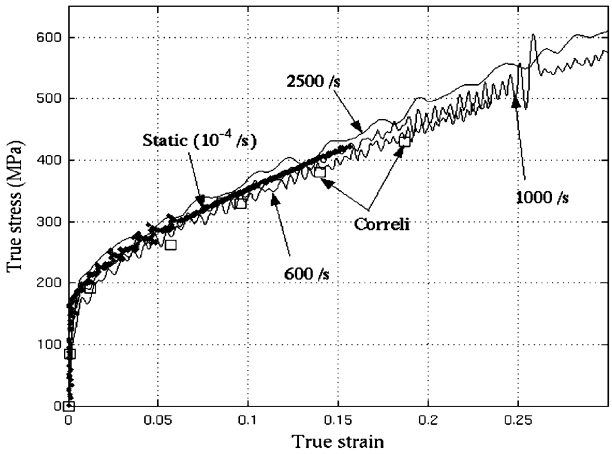

Fig. 3. Stress–strain relations for static and dynamic strain rates.

force–displacement signals. The force–displacement recordings were quite repeatable indicating that the heat-treatment applied is reproducible.

For dynamic loading, the direct impact configuration (Hauser, 1966) with a large scale SHPB system (diameter 80 mm, input bar of 6 m and output bar 4 m) was used to obtain the force and displacement history (Abdennadher et al., 2003). Such measurements allows the study of the successive peak load under impact, which was not possible in previous work where only the final crushing displacement at a given mass and initial velocity were measured (Abramowicz and Jones, 1984, 1986). However, the key difficulty of this arrangement is the long measurement duration needed to observe the successive peak load (after the initial peak load). A two-gauge method (Lundberg and Henchoz, 1977) was used to process the signals after the first round trip of the waves in the bars. Additional details of this measurement method are described in Zhao and Gary (1997) and Bussac et al. (2002).

A typical comparison between static and dynamic tests is shown in Fig. 4. We can see that not only the initial peak load but also the successive peak load were measured. There is a significant enhancement of both the initial and successive peak loads. It can also be seen that the tests under static and dynamic loading are reproducible. Table 1 provides the corresponding initial and successive peak loads under static and impact loads. The average enhancement is about 35% for both initial and successive peak loads.

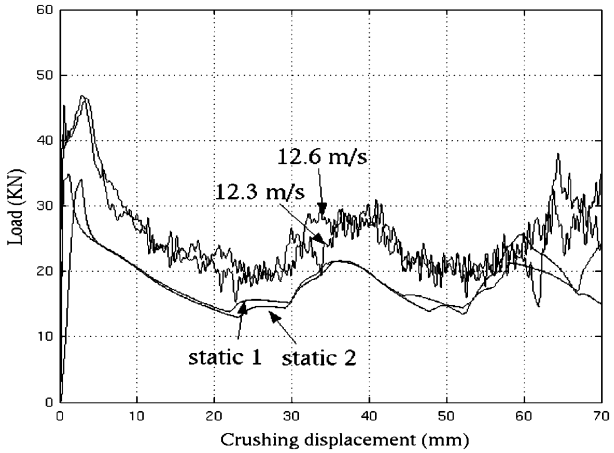

Fig. 4. Force–displacement curves under static and dynamic loading.

Table 1
Enhancement ratio for initial and successive peak loads

Speed (m/s)	Initial peak (kN)	Increase (kN)	Successive peak (kN)	Increase (kN)
Static	**35**		**22**	
7.7	43	9 (26%)	29	7 (32%)
9.6	43	9 (26%)	28	6 (28%)
11	45	11 (31%)	28	6 (28%)
11.5	45	11 (31%)	28	6 (28%)
12.3	46	12 (34%)	29	7 (32%)
12.6	47	13 (37%)	29	7 (32%)
13.5	47	13 (37%)	30	8 (36%)
15.3	49	15 (43%)	31	9 (41%)

3. Numerical analyses of tube crushing

In the crushing tests presented above, only force–displacement recordings were made. For static loading, some pictures were also taken of the tubes during tests. There are no simple methods to know what was happening in the tube, especially under impact loading. An alternative is to simulate the crushing of the tubes numerically, provided that the simulation is able to reproduce the force–displacement history and other recorded data such as pictures. Under such conditions, numerical simulation may give reliable local information, such as the stress state and deformation history in the tube.

3.1. Validity of numerical models

The explicit version of the commercial code LS-DYNA was used to perform the simulations under impact loading, and the implicit version was adopted for static loading. The velocity–time histories of both tube sides (measured velocities in both static and dynamic cases) were imposed by two rigid walls. A "contact_automatic_single_surface" interface was used to avoid interpenetration.

For the simulation with the explicit version, the Belytscheko & Tsai plate elements with 3 points of integration through the thickness was used. Flanagan–Belytschko stiffness form hourglass control was applied with a coefficient of 0.05. For the constitutive equation, the simple Johnson–Cook law parameters were identified from experimental stress–strain curves obtained from compressive tests on small specimens. The parameters A, B, n were respectively determined as 150 MPa, 820 MPa and 0.62. The parameters for the rate sensitivity and the temperature effect were chosen to be zero. For the simulation with the implicit version, the quasi-Newton method with BFGS stiffness updating was used. More detailed information about the simulation method can be found in the LS-DYNA manual (Halquist, 1991).

The same geometry file were used in both static and dynamic loading to reduce numerical errors. The sensitivity of the simulated results to the mesh density was analyzed in order to choose a suitable element size for the simulation. The chosen element size was 2.5×2.5 mm, which gives 14 elements in each side. It corresponds roughly to the rule of 7 elements in a half wave length. The use of smaller elements was found not to make a significant difference.

The simulated results of the tube crushing strongly depended on the initial imperfection introduced in the geometry of the tube. Random and sinusoidal perturbations of the wall geometry were used. Sinusoidal perturbations were found to be more numerically stable at initiating the symmetric successive mode observed in all our tests. Sinusoidal perturbations with a half wave length of 26.25 mm were then used in our simulations. The amplitude of the perturbation is also an important parameter. In the present case, the maximum lateral perturbation was chosen to be 0.08 mm, for around this value the peak loads are nearly unaffected. Fig. 5a gives a comparison between experimental and simulated force–displacement curves under static loading. It illustrates that the numerical calculation gives a fair estimation of the force as well as the displacement.

Fig. 5b provides a comparison between the force–time histories of the rigid wall under both static and dynamic loading. The simulated crushing tests also reproduce the strength enhancement under dynamic loading not only for the initial peak load but also for the successive peak load, which is another proof of the value of simulations. However, this simulated enhancement for the successive peak load is not as strong as that in the real tests (compare Figs. 4 and 5b). This is due to the imprecision of the simulation for dynamic loading.

Fig. 6 shows a comparison between pictures taken during static tests (on the left) with the corresponding simulations. A good match between these images shows that simulation gives a good prediction of successive crushing. Such comparisons show that the simulations (with previously specified element size and mode and amplitude of the initial geometrical perturbation) provide a reliable description of tube crushing. It therefore functions as a virtual test, through which the user has access to global and local stresses and strains at any chosen time for understanding the crushing mechanisms.

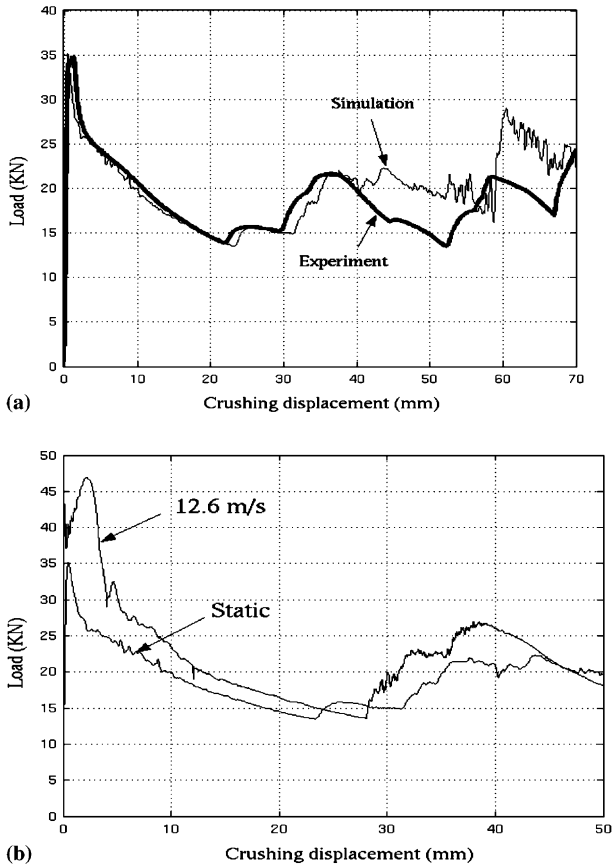

Fig. 5. (a) Experimental and simulated force–displacement curves. (b) Simulated force–displacement curves under static and dynamic loading.

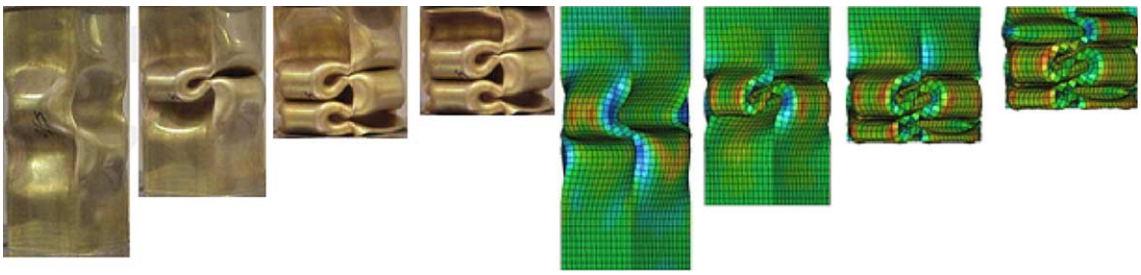

Fig. 6. Comparison of experimental (4 images on the left) and simulated images.

3.2. Folding events

A careful examination of the sequence of events in successive crushing reveals that the folding cycles are composed of two stages. At the start, crush is obtained by bending in the middle of the flat plates (the two trapezoids around nodes B or B′ in Fig. 7) and there exist small areas around the four corner lines (the two

adjacent triangles around node A in Fig. 7) which remain vertical (no significant lateral displacement). In the simulated images of a deformed tube (left part of Fig. 7), the corner line between the two triangles around node A is straight whereas the flat plate is already bent. Subsequently, the second stage begins with the buckling of the corner line areas as shown on the right of Fig. 7.

The buckling of these edge zones (the two adjacent triangles around node A in Fig. 7) corresponds to a decrease of the global crushing load. Fig. 8 shows the displacement in two perpendicular lateral directions at node A at the corner with the corresponding global crushing force. The displacement value of 41 mm corresponds to the time when the corner node begins to move laterally and the global crushing force begins to decrease. Furthermore, Fig. 9 shows the profile of lateral displacement of an adjacent plate starting from the middle (point B, Fig. 7) to the corner (point A, Fig. 7) at this moment. It can be seen that just before the force decreases, the corner elements are not laterally displaced whereas the central element has already moved laterally in both static and dynamic cases.

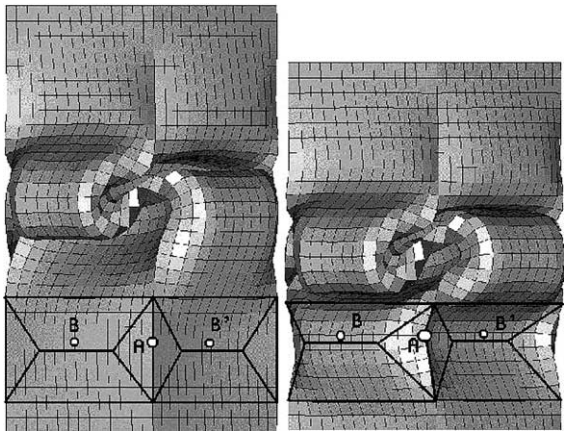

Fig. 7. Detail of simulated deformed tubes.

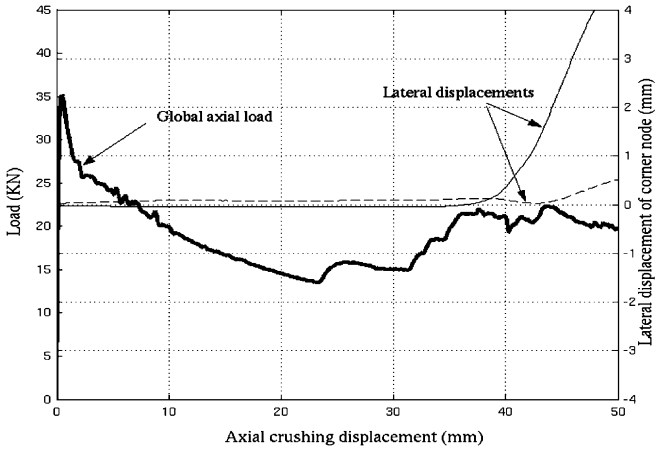

Fig. 8. Lateral displacement of corner node and global crushing force.

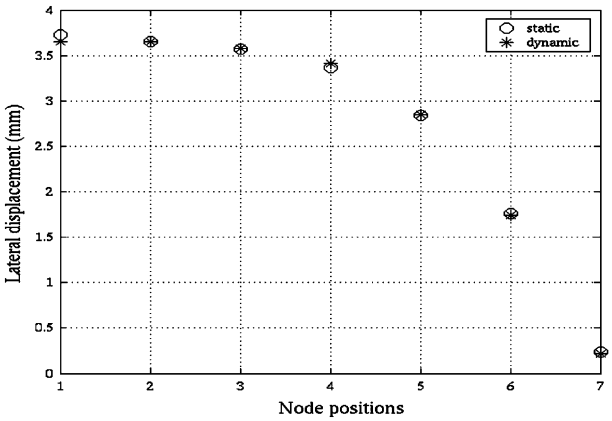

Fig. 9. Lateral displacement of 7 elements across the half width of the flat plate (position 1 denotes the element in the middle of the flat plate, position 7 the element in the corner line).

An idealized crushing kinematical box model is shown in Fig. 10. The crushing process can be divided into two stages. The first is mainly bending of the central plates in an X-form, one plate bends outwards and the adjacent plate bends inwards. Kinematical compatibility can be obtained by the rotation of two adjacent triangular elements along with their vertical compression. The second phase is the buckling of these 8 angular elements around the four edges.

It is also interesting to check the stress profile in the crushing direction, e.g., in the cross-section from node B to node A (see Fig. 7). This shows that the corner element supports most of the crushing load (Fig. 11). This explains why the buckling force of these zones determines the peak loads in the successive folding process. Similar conclusions can be drawn for the static as well as the dynamic cases. In Fig. 11, it can also be seen that there is nearly no variation for the central elements with rate. An enhancement of 14% is observed for the corner elements corresponding roughly to the rigid wall force enhancement between the static and dynamic simulations shown in Fig. 5b.

Fig. 12 shows that, the von Mises equivalent strain profile in the dynamic case is higher than in the corresponding static case, and this is especially true for the corner elements. It reveals that in the regions close to the edge, elements are more compressed (higher strain) under dynamic loading because of inertia, This is similar to what was found for a straight column. As the base material (brass) strain hardens, a higher strain is reached under dynamic loading before buckling leading to higher crushing forces.

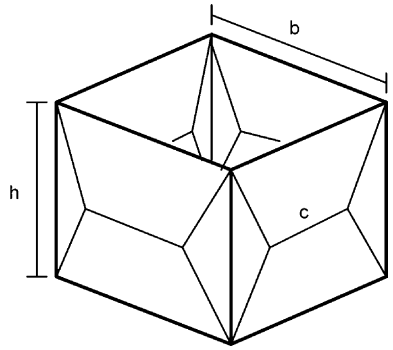

Fig. 10. Model for box column crushing.

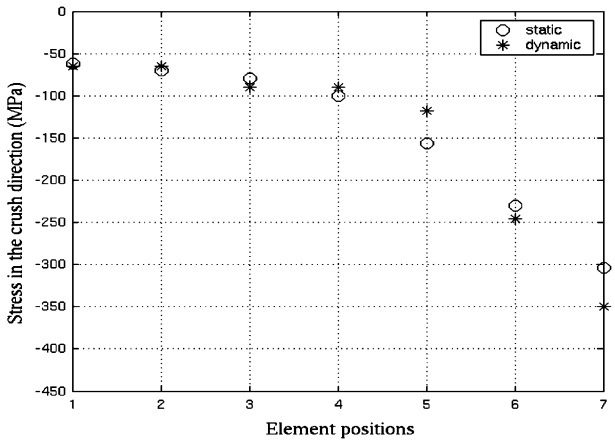

Fig. 11. Stress profile in the crushing direction from centre to corner (position 1 denotes the element in the middle of the flat plate, position 7 the element in the ridge line).

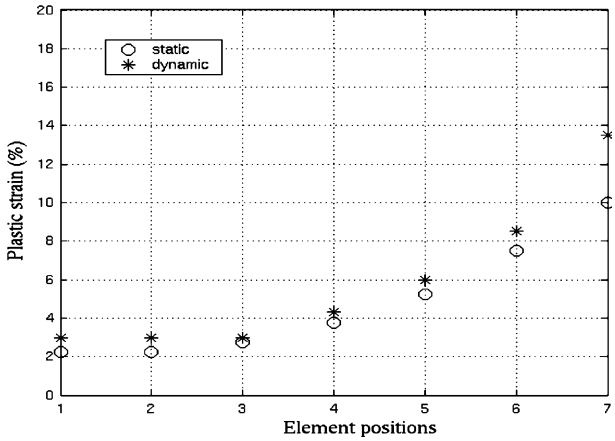

Fig. 12. Residual strain profile from middle to corner (position 1 denotes the element in the middle of the flat plate, position 7 the element in the ridge line).

4. Theoretical analysis of an idealized box column model

From the kinematical box model shown in Fig. 10, it is possible to derive a theoretical analysis. A similar box model has been used by many authors (Abramowicz and Wierzbicki, 1989; Wierzbicki and Huang, 1991; Markiewicz et al., 1996; Meng et al., 1983). Fig. 13 shows the case where this idealized buckling box has a wavelength equal to b and the middle length of the X element equal to $b/2$.

In this simplified crushing model, the middle length is fixed during the whole crushing cycle. Therefore, the effect of stretching and travelling hinges (Johnson et al., 1977; Wierzbicki and Bhat, 1986) cannot be taken into account. However, stretching is much less important than axial compression in terms of energy balance; and compared to a fixed hinge, travelling hinges mainly spread out the same quantity of bending energy. These effects play an important role in finding the right kinematical crushing mode and

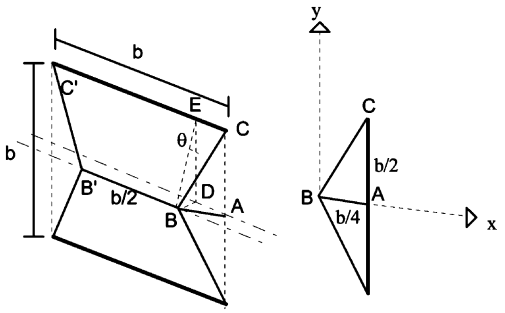

Fig. 13. More detailed crushing box column model.

consequently the whole energy absorption in a whole cycle, but they are not significant for the energy balance at a given instant where the kinematical mode is already assumed. As the crushing mode in our case is imposed by experimental observation for both static and dynamic loading, these effects can be reasonably neglected in the energy balance for this given kinematical mode at a given instant.

4.1. First peak load

The initial peak load increases with increase of impact velocity. The nominal stress can be calculated by dividing the crushing force by the cross-section of the tube. This nominal stress follows the stress–strain curve of the base material as predicted by the theory of buckling of a straight column (Fig. 14). The initial peak load is determined by the compressive load at the time when the structure departs from simple compression loading.

The initial peak load for the static case can be estimated by multiplying the flow stress at the buckling strain by the tube cross-sectional area. Under static loading, the strain at buckling is about 1.5% corresponding to a flow stress of about 175 MPa. This leads to the following estimate:

$$F^{\text{static}}_{\text{initial peak}} = \sigma_s A = 175\ \text{MPa} \times 201\ \text{mm}^2 \approx 35\ \text{kN}$$

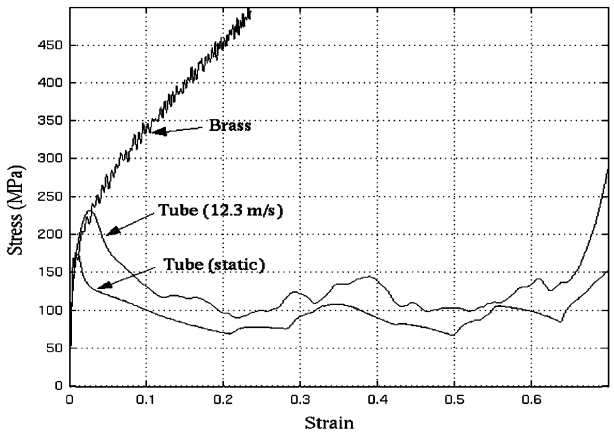

Fig. 14. Force divided by cross-section area vs. displacement divided by length.

Under impact loading, inertia leads to a larger buckling strain of 3% and a corresponding flow stress of about 225 MPa, so that

$$F_{\text{initial peak}}^{\text{impact}} = \sigma_s A = 225\ \text{MPa} \times 201\ \text{mm}^2 \approx 46\ \text{kN}$$

Using the idealized box column model of Fig. 13 for a given small angle θ corresponding to about 2% of strain, one can apply a small perturbation to this state (just *after* initial buckling) to obtain an energy balance analysis. The energy increment is contributed by the 4 X-shaped bending element and 8 triangular corner elements. The total energy increment is thus the sum of the 8 trapezoids BB′CC′ and the 16 triangles ABC.

Let us consider a small virtual crushing increment δv, which is a vertical displacement of the line CC′ with respect to the symmetrical central line BB′. A uniform strain state in the triangle is assumed in calculating the energy increment for one of the 16 triangular elements (ABC). For incompressible plasticity, it leads to the following strain state (see Appendix A):

$$\delta\varepsilon^{\text{p}} = \begin{bmatrix} 0 & \dfrac{\delta v}{b/2} & 0 \\ \dfrac{\delta v}{b/2} & \dfrac{\delta v}{b/2} & 0 \\ 0 & 0 & -\dfrac{\delta v}{b/2} \end{bmatrix} \tag{4}$$

and results in the following equivalent strain: $\delta\varepsilon_{\text{eq}}^{\text{p}} = 4\sqrt{\frac{2}{3}}\frac{\delta v}{b}$.

The energy increment is the sum of the product of the flow stress and the equivalent strain increment of all the small triangles (Eq. (A.4) in Appendix A):

$$\Delta E_{\text{triangle}} = 4\sigma_s\sqrt{\frac{2}{3}}\delta v b t \tag{5}$$

where σ_s, t denote the flow stress and the wall thickness.

By assuming that the energy absorbing part of the X-shaped elements is just the plastic hinge lines (CC′, BB′, BC, B′C′) and that the plate is free from compression or shear, a perturbation rotation of $\delta\theta$ about the hinge line CC′ leads to a rotation $2\delta\theta$ about the hinge line BB′. In the present situation, the hinge lines BC and B′C′ will rotate by $\delta\varphi$.

The whole bending energy of the square box can therefore be defined as follows:

$$\Delta E_{\text{bending}} = 8\left[m_{\text{p}}\delta\theta b + m_{\text{p}}\delta\theta b/2 + 2m_{\text{p}}\delta\varphi\sqrt{5}\frac{b}{4}\right] \tag{6}$$

where $m_{\text{p}} = \frac{t^2\sigma_s}{4}$ is the plastic moment per length unit within the hinge line.

Using the geometric relation between the vertical displacement and the rotation angle in Eq. (2), the bending energy increment is finally (see Eq. (B.4) in Appendix B),

$$\Delta E_{\text{bending}} = (3 + 3\sqrt{5})\sigma_s t^2\frac{2\delta v}{\sin\theta} \tag{7}$$

The energy balance is written as:

$$2F\delta v = (3 + 3\sqrt{5})\sigma_s t^2\frac{2\delta v}{\sin\theta} + \sigma_s 4\sqrt{\frac{2}{3}}\delta v b t \tag{8}$$

so that the applied load becomes

$$F = 3(1 + \sqrt{5})\sigma_s\frac{t^2}{\sin\theta} + \sigma_s 2\sqrt{\frac{2}{3}}bt \tag{9}$$

The angle θ is related to the edge line variation ratio (i.e. strain for the ridge element) by the following relationship:

$$\cos\theta = (b - b\varepsilon)/b, \quad \text{where } \varepsilon \text{ is the strain at the edge line} \tag{10}$$

At the moment just after initial buckling, the edge line strain is about 2% (see Fig. 14) implying an angle of 11°. In the present case, $b = 35$ mm, $t = 1,5$ mm, $\sigma_s = 175$ MPa (static case), we have:

$$F^{\text{static}}_{\text{initial peak}} \approx 114\ \text{mm}^2\sigma_s + 85\ \text{mm}^2\sigma_s \approx 35\ \text{kN} \tag{11a}$$

Eq. (11a) shows that at this strain (2%), the bending model outlined gives the same crushing load as that for pure compression considered previously. It means therefore, that the initial peak load corresponds to the buckling of X-shaped elements in the centre of each plate. The simplified crushing kinematics is thereby confirmed. Eq. (11a) provides also the respective contributions of the bending part (first term) and the triangular elements (second term).

Inertia under impact loading leads to an increased strain (and higher flow stress $\sigma_s = 225$ MPa) before buckling and consequently to a higher initial peak load.

$$F^{\text{impact}}_{\text{initial peak}} \approx 114\ \text{mm}^2\sigma_s + 85\ \text{mm}^2\sigma_s \approx 45\ \text{kN} \tag{11b}$$

4.2. Successive peak load

However, our interest is the successive peak load because it is the basis of the crushing strength enhancement for cellular structures. The simulations presented in Section 3 showed that buckling of the vertically straight triangular elements determines the successive peak load. One should analyze further crushing of the idealized crushing box shown in Fig. 13 by further bending of X-shaped central plates and compression-shear of the straight triangular elements.

Let us consider the moment just before the buckling of these straight triangular elements. The angle θ is 28.4° for a edge line strain of 12% (see Fig. 12).

From the simulated results (Fig. 12), further crushing leads to a linear distribution of the strain and stress in the triangular elements. By assuming that a further drop of point C will induce a linear plastic strain distribution, the strain increment becomes (see Appendix A)

$$\delta\varepsilon^{\text{p}}(x) = \begin{bmatrix} 0 & \dfrac{\delta v}{b/2} & 0 \\ \dfrac{\delta v}{b/2} & \dfrac{\delta v}{b/2} & 0 \\ 0 & 0 & -\dfrac{\delta v}{b/2} \end{bmatrix} \frac{4x}{b} \tag{12}$$

The flow stress is also assumed to be a linear function of x (see Fig. 11). It varies from σ_s (the compression flow stress just before the initial peak load as used in Eq. (11)) to σ'_s (maximum flow stress at the edge line before the successive folding peak load). The energy increment in these small triangles is then given by Eq. (13) (see Eq. (A.7) in Appendix A).

$$\Delta E_{\text{triangle}} = 2\sigma'_s\sqrt{\frac{2}{3}}bt + \sigma_s\frac{2}{3}\sqrt{\frac{2}{3}}bt \tag{13}$$

The bending energy increment is defined according to Eq. (6) (see Eq. (B.7) in Appendix B)

$$\Delta E_{\text{bending}} = (3 + 2\sqrt{5})\sigma_s t^2\frac{2\delta v}{\sin\theta} \tag{14}$$

Table 2
Comparison between the model and experiments

	$F^{\text{static}}_{\text{initial peak}}$ (kN)	$F^{\text{impact}}_{\text{initial peak}}$ (kN)	$F^{\text{static}}_{\text{successive peak}}$ (kN)	$F^{\text{impact}}_{\text{successive peak}}$ (kN)
Model	35	46	23	29
Experiment	35	45	22	29

The energy balance yields:

$$F = (3 + 2\sqrt{5})\sigma_s \frac{t^2}{\sin\theta} + \sigma'_s \sqrt{\frac{2}{3}} bt + \sigma_s \frac{1}{3}\sqrt{\frac{2}{3}} bt \tag{15}$$

Therefore, in the present case, $b = 35$ mm, $t = 1.5$ mm, $\sigma_s = 175$ MPa, $\sigma'_s = 350$ MPa (see Figs. 3 and 14), so that:

$$F^{\text{static}}_{\text{successive peak}} \approx 35\ \text{mm}^2\sigma_s + 42\ \text{mm}^2\sigma'_s + 14\ \text{mm}^2\sigma_s \approx 23\ \text{kN} \tag{16a}$$

Under dynamic loading, the strain is increased before buckling, which leads to $\sigma_s = 225$ MPa, $\sigma'_s = 425$ MPa, and therefore

$$F^{\text{impact}}_{\text{successive peak}} \approx 35\ \text{mm}^2\sigma_s + 42\ \text{mm}^2\sigma'_s + 14\ \text{mm}^2\sigma_s \approx 29\ \text{kN} \tag{16b}$$

Table 2 gives a comparison between model estimates and experimental results.It offers a good explanation of the successive peak load. Eqs. (16a) and (16b) provide also the respective contributions of the X-shaped bending elements (first terms) and of the triangular elements. The bending part is relatively small and the vertically straight triangular elements take more than 80% of the crushing load.

5. Post-mortem micro-hardness measurement for validation

The above simulations and analyses suggest that strain hardening of the base material combined with inertia is the origin of the strength enhancement under dynamic loading. To prove that, micro-hardness tests on the crushed tubes at various crushing stages were performed. The micro-hardness of the material reveals its average strain hardening state. It therefore provides an experimental check of the local strain profile given by the simulation.

However, it is also known that hardness measurements and plastic strain are not directly and quantitatively related so reference tests on the base material for a series of given strain levels were performed and an empirical relationship was derived for this material under such loading.

The strain state of the small specimens used to investigate brass rate sensitivity are known (Fig. 3). Post-mortem micro-hardness measurement on these small specimens gave a correspondence between the micro-hardness and the known plastic strain. This correspondence for heat-treated brass material is shown in Fig. 15. The same micro-hardness measurement was then applied to the square tubes.

Qualitative and quantitative matching was then sought between the simulations and the experiments. Fig. 16 shows a typical micro-hardness measurement operation. Three crushing states under static loading were used for this matching. The first is the one just after the first peak load (16a left), the second is the one just after the second peak load, which is the successive peak load (middle). The last one corresponds to the case after full crushing (right). Figs. 16b and 16c show the specimen preparation and an indentation mark from a micro-hardness measurement. It should be noted that the measurements presented in Fig. 16d were made in the middle of the plate (half thickness position). The hardness near the plate surfaces is quite different because of bending effects.

Such measurements prove that (i) just after the first initial peak load, the plastic strain is nearly uniform in a section. (ii) Afterwards, only the region near the corner line is loaded. These observations confirm the

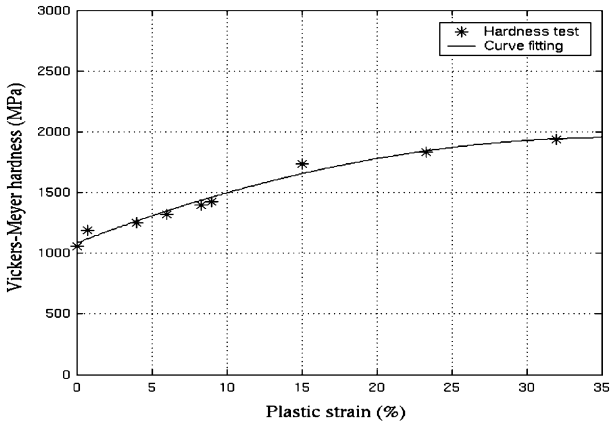

Fig. 15. Micro-hardness vs. plastic strain.

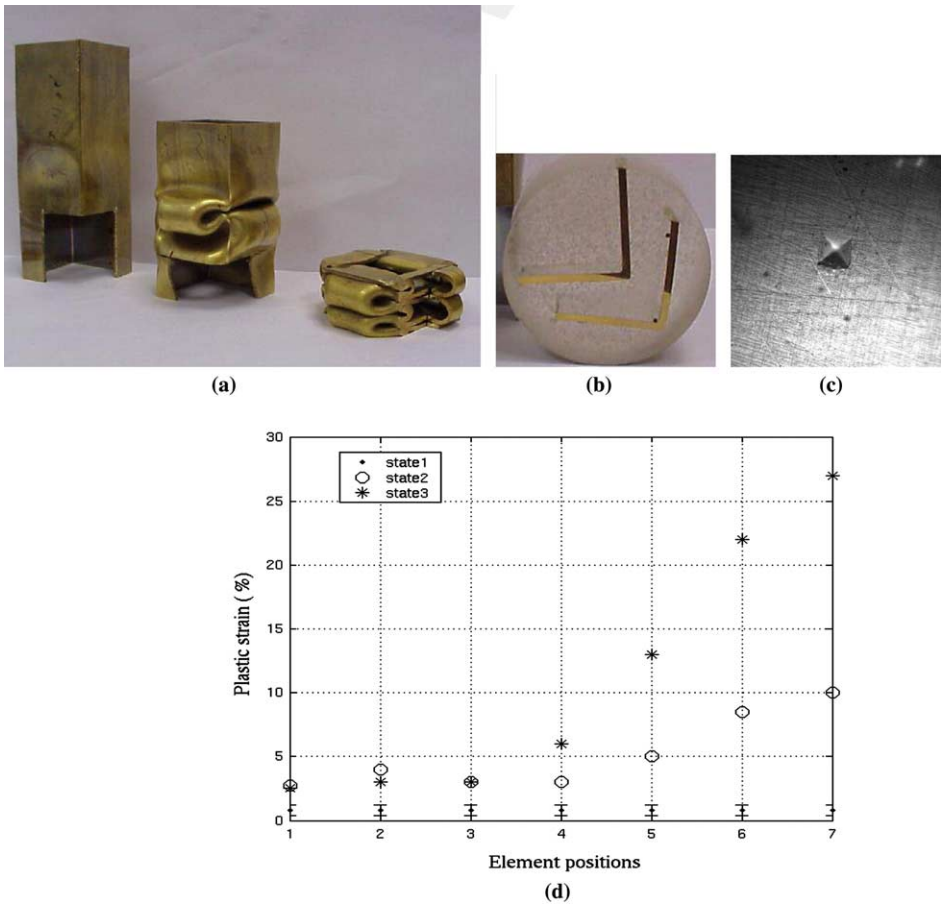

Fig. 16. (a) Crushed tubes, (b) prepared piece for hardness measurement, (c) stamp and (d) plastic strain profiles at three crushing stages (position 1 denotes the element in the middle of the flat plate, position 7 the element in the ridge line).

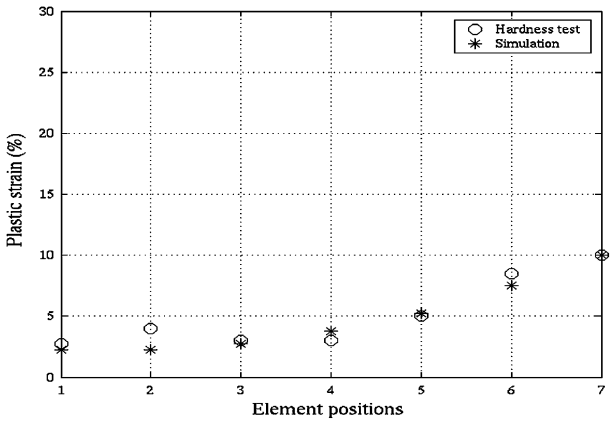

Fig. 17. Comparison simulation and micro-hardness measurement (position 1 denotes the element in the middle of the flat plate, position 7 the element in the ridge line).

theory developed above. Furthermore, an excellent match between simulation and post-mortem micro-hardness measurement was found (Fig. 17), validating the results given by the simulations.

6. Summary

This paper analyzes the strength enhancement under impact loading of annealed brass square tubes under a symmetric successive folding mode. The key points are the following:

(i) Using a large scale (80 mm diameter, and 10 m long) SHPB system, the successive folding peak loads under impact (8–15 m/s) were measured. A 35% increase of the successive folding peak load was observed for tubes made of rate insensitive materials.
(ii) Numerical simulations show that the crushing force in successive folding is supported by two distinct mechanisms : the bending of the plate in a X-shape between two adjacent edges and compression and shear in triangular elements around the four edges of the square tubes. These triangular elements under compression and shear support 80% of the crushing force. This crushing force reaches its maximum in a folding cycle (successive peak load) when these triangular elements begin to buckle.
(iii) The analytical model of a box column crushing presented gives an explanation of the observed strength enhancement. (A) The successive peak load depends on the moment the buckling of the triangular elements around the four edges occurs. (B) Buckling is delayed under impact loading because of inertia leading to an increase in the strain reached before buckling occurs in these triangular elements. (C) Stresses in these elements (and consequently the crushing force) are higher because of strain hardening even if the material is not rate sensitive.
(iv) Post-mortem micro-hardness measurements of tubes at different crushing stages confirm this conclusion.

This study shows that square tubes made of rate insensitive but strain hardening materials exhibit significant strength enhancement under impact loading because of inertia effects. It may provides an explanation of the strength enhancement of cellular structures, the deformation mode of which is successive folding of cell walls.

Appendix A. Calculation of energy increment in the triangular element

By assuming that the strain field is uniform, the vertical compression is related to the vertical displacement δv of the point C (Fig. 13) by Eq. (A.1a).

$$\delta\varepsilon^{\mathrm{p}}_{yy} = \frac{\delta v}{\frac{b}{2}} \tag{A.1a}$$

The out-of-plan displacement of line AB necessary for the kinematical compatibility leads to an in-plan horizontal stretch and a shear. If we assume that the stretching is negligible ($\delta\varepsilon^{\mathrm{p}}_{xx} = 0$), there are then only vertical compression and shear This shear component (Wierzbicki and Huang, 1991) is approximatively evaluated by Eq. (A.1b).

$$\delta\varepsilon^{\mathrm{p}}_{xy} = \frac{1}{2}\frac{\delta v}{\frac{b}{4}} \tag{A.1b}$$

Note that $b/2$ and $b/4$ are respectively the lengths AC and AB of the triangle ABC (Fig. 13). To ensure incompressibility in plasticity, a plastic strain in the thickness is assumed

$$\delta\varepsilon^{\mathrm{p}}_{zz} = -\delta\varepsilon^{\mathrm{p}}_{yy}$$

This leads to the following form of the strain increment

$$\delta\varepsilon^{\mathrm{p}} = \begin{bmatrix} 0 & \dfrac{\delta v}{b/2} & 0 \\ \dfrac{\delta v}{b/2} & \dfrac{\delta v}{b/2} & 0 \\ 0 & 0 & -\dfrac{\delta v}{b/2} \end{bmatrix} \tag{A.2}$$

resulting in the following equivalent strain

$$\delta\varepsilon^{\mathrm{p}}_{\mathrm{eq}} = 4\sqrt{\frac{2}{3}}\frac{\delta v}{b} \tag{A.3}$$

If σ_{s}, t denote the flow stress and the wall thickness respectively, the energy increment in all the small triangles is

$$\Delta E_{\mathrm{triangle}} = 16\left[\int_V \sigma_{\mathrm{s}}\delta\varepsilon^{\mathrm{p}}_{\mathrm{eq}}\mathrm{d}\Omega\right] = 16\sigma_{\mathrm{s}}4\sqrt{\frac{2}{3}}\frac{\delta v}{b}\frac{b^2 t}{16} \tag{A.4}$$

For the successive peak load, it is assumed that the strain state is linear in the direction of x:

$$\begin{aligned} &\delta\varepsilon^{\mathrm{p}}_{xx} = 0 \\ &\delta\varepsilon^{\mathrm{p}}_{yy} = \frac{\delta v}{\frac{b}{2}}\frac{x}{\frac{b}{4}} \quad \delta\varepsilon^{\mathrm{p}}_{xy} = \frac{1}{2}\frac{\delta v}{\frac{b}{4}}\frac{x}{\frac{b}{4}} \end{aligned} \tag{A.5}$$

The strain state for an incompressible plasticity is then given by the following expression:

$$\delta\varepsilon^{\mathrm{p}}(x) = \begin{bmatrix} 0 & \dfrac{\delta v}{b/2} & 0 \\ \dfrac{\delta v}{b/2} & \dfrac{\delta v}{b/2} & 0 \\ 0 & 0 & -\dfrac{\delta v}{b/2} \end{bmatrix}\frac{4x}{b} \tag{A.6}$$

This permits the calculation of the equivalent strain and with a linear distribution of the flow stress from σ_s to σ'_s.

$$\Delta E_{\text{triangle}} = 16\left[\int_V \left[(\sigma'_s - \sigma_s)\frac{4x}{b} + \sigma_s\right]\delta\varepsilon^p_{eq}(x)\mathrm{d}\Omega\right] = 16\left[4\sqrt{\frac{2}{3}}\frac{\delta v}{b}\left[(\sigma'_s - \sigma_s)\frac{b^2 t}{32} + \sigma_s\frac{2}{3}\frac{b^2 t}{16}\right]\right]$$
$$= 2\sigma'_s\sqrt{\frac{2}{3}}bt + \sigma_s\frac{2}{3}\sqrt{\frac{2}{3}}bt \tag{A.7}$$

Appendix B. Calculation of the energy increment in X-shaped bending element

To calculate the bending energy increment in the X-shaped element, the relationship between $\delta\varphi$ and $\delta\theta$ is needed (Fig. 18).

φ denotes the angle between triangles BCE and ABC. The normal directions of the triangle BCE and ABC are respectively:

$$n1 = \begin{bmatrix}\cos\theta \\ 0 \\ \sin\theta\end{bmatrix} \quad n2 = \begin{bmatrix}\cos 2\theta \\ \sin 2\theta \\ 0\end{bmatrix} \tag{B.1}$$

The angle φ can be calculated by

$$\cos\varphi = n1 \cdot n2 = \cos\theta\cos 2\theta \tag{B.2}$$

For a very small angle, we can make the following approximation:

$$\varphi = 3\theta \quad \text{and} \quad \delta\varphi = 3\delta\theta \tag{B.3}$$

For the general case, we have the following differential relation.

$$\sin\varphi\delta\varphi = (\sin\theta\cos 2\theta + 2\cos\theta\sin 2\theta)\delta\theta \tag{B.4}$$

Geometric relations between the vertical displacement and the rotation angle in Eq. (2) leads to the following relation between the angle $\delta\theta$ and δv

$$\delta\theta = 2\delta v/b\sin\theta \tag{B.5}$$

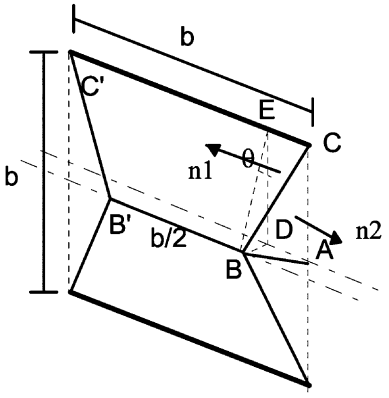

Fig. 18. Relationship between rotation angles θ and φ.

Using Eq. (B.3) for the case of small angles for the initial peak load, the bending energy increment is

$$\Delta E_{\text{bending}} = 8\left[m_{\text{p}}\delta\theta b + m_{\text{p}}\delta\theta b/2 + 2m_{\text{p}}\delta\varphi\sqrt{5}\frac{b}{4}\right] = (3+3\sqrt{5})\sigma_{\text{s}}t^2\frac{2\delta v}{b\sin\theta}b \tag{B.6}$$

For the angle $\theta = 28.4°$ in the case of successive peak load, Eq. (B.4) leads to $\delta\varphi \cong 2\delta\theta$.

The bending energy increment is then

$$\Delta E_{\text{bending}} = 8\left[m_{\text{p}}\delta\theta b + m_{\text{p}}\delta\theta b/2 + 2m_{\text{p}}\delta\varphi\sqrt{5}\frac{b}{4}\right] = (3+2\sqrt{5})\sigma_{\text{s}}t^2\frac{2\delta v}{b\sin\theta}b \tag{B.7}$$

References

Abdennadher, S., 2004. Etude de l'écrasement de structures alvéolaires sous sollicitations dynamiques rapide: Application aux matériaux cellulaires. Ph.D Thesis, University of Paris 6.

Abdennadher, S., Zhao, H., Othman, R., 2003. Cellular structures under impact loading. Journal de Physique IV 110,, 441–446.

Abramowicz, W., Jones, N., 1984. Dynamic axial crushing of square tubes. International Journal of Impact Engineering 2 (2), 179–208.

Abramowicz, W., Jones, N., 1986. Dynamic successive buckling of circular and square tubes. International Journal of Impact Engineering 4 (4), 243–270.

Abramowicz, W., Wierzbicki, T., 1989. Axial crushing of multicorner sheet metal columns. Journal of Applied Mechanics 56, 113–120.

Banhart, J., 2001. Manufacture, characterisation and application of cellular metals and metal foams. Progress in Material Science 46, 559–632.

Budiansky, B., Hutchinson, J.W., 1964. Dynamic buckling of imperfection sensitive structures. In: Proceedings of 11th international Congress of Applied Mechanics. Springer Verlag, Munich.

Bussac, M.N., Collet, P.C., Gary, G., Othman, R., 2002. An optimisation method for separating and rebuilding one-dimensional dispersive waves from multi-point measurements. Application to elastic or viscoelastic bars. Journal of Mechanics and Physics of Solids 50, 321–349.

Calladine, C.R., English, R.W., 1984. Strain-rate and inertia effects in the collapse of two types of energy-absorbing structure. International Journal of Mechanical Science 26 (11–12), 689–701.

Chevalier, L., Calloch, S., Hild, F., Marco, Y., 2001. Digital image correlation used to analyse the multiaxial behavior of rubber-like materials. European Journal of Mechanics A/Solids 20, 169–187.

Davies, R.M., 1948. A critical study of Hopkinson pressure bar. Philosophical Transaction of Royal Society A 240, 375–457.

Deshpande, V.S., Fleck, N.A., 2000a. Isotropic constitutive models for metallic foams. Journal of Mechanics and Physics of Solids 48, 1253–1283.

Deshpande, V.S., Fleck, N.A., 2000b. High strain rate compression behaviour of aluminium alloy foams. International Journal of Impact Engineering 24, 277–298.

Gary, G., 1983. Dynamic buckling of an elastoplastic column. International Journal of Impact Engineering 2, 357–375.

Gibson, L.J, Ashby, M.F, 1988. Cellular Solids. Pergamon Press.

Goldsmith, W., Sackman, J.L., 1992. An experimental study of energy absorption in impact on sandwich plates. International Journal of Impact Engineering 12 (2), 241–262.

Halquist, J.O., 1991. LS-DYNA theoretical manual, Livermore Software Technology Corporation.

Hauser, F.E., 1966. Techniques for measuring stress–strain relations at high strain rates. Experimental Mechanics 6, 395–402.

Hanssen, A.G., Hopperstad, O.S., Langseth, M., Ilstad, H., 2002. Validation of constitutive models applicable to aluminium foams. International Journal of Mechanical Sciences 44 (2), 359–406.

Hild, F., Périé, J.N., Coret, M., 1999. Mesure de champs de déplacements 2D par intercorrélation d'images. CORRELI2D, LMT-Cachan, internal report no. 230.

Hopkinson, B., 1914. A method of measuring the pressure in the deformation of high explosives or by the impact of bullets. Philosophical Transaction of Royal Society A 213, 437–452.

Johnson, W., Soden, P.D., Al-Hassani, S.T.S., 1977. Inextensional collapse of thin-walled tubes under axial compression. Journal of Strain Analysis 12, 317–330.

Karagiozova, D., Alves, M., Jones, N., 2000. Inertia effects in axisymmetrically deformed cylindrical shells under axial impact. International Journal of Impact Engineering 24, 1083–1115.

Klintworth, J.W., Stronge, W.J., 1988. Elasto-plastic yield limits and deformation laws for transversely crushed honeycombs. International Journal of Mechanical Science 30 (3–4), 273–292.

Kolsky, H., 1949. An investigation of the mechanical properties of materials at very high rates of loading. Proceeding of Physical Society B 62, 676–700.

Langseth, M., Hopperstad, O.S., 1996. Static and dynamic axial crushing of square thin-walled aluminium extrusions. International Journal of Impact Engineering 18 (7–8), 949–968.

Langseth, M., Hopperstad, O.S., Berstad, T., 1999. Crashworthiness of aluminium extrusions : validation of numerical simulation, effect of mass ratio and impact velocity. International Journal of Impact Engineering 22, 829–854.

Lundberg, B., Henchoz, A., 1977. Analysis of elastic waves from two-point strain measurement. Experimental Mechanics 17, 213–218.

Markiewicz, E., Ducrocq, P., Drazetic, P., Ravalard, Y., 1996. Calculation of the dynamic axial crushing response of complex prismatic sections. International Journal of Crashworthiness 1, 203–224.

Meng, Q., Al-Hassani, S.T.S., Soden, P.D., 1983. Axial crushing of square tubes. International Journal of Mechanical Science 25, 747–773.

Mukai, T., Kanahashi, H., Miyoshi, T., Mabuchi, M., Nieh, T.G., Higashi, K., 1999. Experimental study of energy absorption in a closed cell aluminium foam under dynamic loading. Scripta Materialia 40 (8), 921–927.

Oguni, K., Ravichandran, G., 2000. An energy-based model of longitudinal splitting in unidirectional fibre reinforced composites. Transaction ASME, Journal of Applied Mechanics 67, 437–443.

Oguni, K., Ravichandran, G., 2001. Dynamic compressive behavior of unidirectional E glass/vinylester composites. International Journal of Mechanical Science 36, 831–838.

Reid, S.R., Peng, C., 1997. Dynamic uniaxial crushing of wood. International Journal of Impact Engineering 19 (5–6), 531–570.

Su, X.Y., Yu, T.X., Reid, S.R., 1995. Inertia sensitive impact energy-absorbing structures part I : Effects of inertia and elasticity. International Journal of Impact Engineering 16 (4), 651–672.

Tan, P.J., Harrigan, J.J., Reid, S.R., 2002. Inertia effects in uniaxial dynamic compression of a closed cell aluminium alloy foam. Material Science & Technology 18, 480–488.

Tam, L.L., Calladine, C.R., 1991. Inertia and strain rate effects in a simple plate structure under impact loading. International Journal of Impact Engineering 11, 689–701.

Vural, M., Ravichandran, G., 2003. Dynamic response and energy dissipation characteristics of balsa wood: experiment and analysis. International Journal of Solids and structures 40, 2147–2170.

Wierzbicki, T., 1983. Crushing analysis of metal honeycombs. International Journal of Impact Engineering 1 (2), 157–174.

Wierzbicki, T., Bhat, S.U., 1986. A moving hinge solution for axisymmetric crushing of tubes. International Journal of Mechanical Science 28, 135–151.

Wierzbicki, T., Huang, J., 1991. Initiation of plastic folding mechanism in crushed box column. Thin Walled Structures 13, 115–143.

Wu, E., Jiang, W.S., 1997. Axial crush of metallic honeycombs. International Journal of Impact Engineering 19 (5–6), 439–456.

Zhao, H., 2004, Cellular materials under impact loading, IFTR-AMAS Edition, Warsaw, Poland. ISSN 1642-0578.

Zhao, H., Gary, G., 1995. A three dimensional analytical solution of longitudinal wave propagation in an infinite linear viscoelastic cylindrical bar. Application to experimental techniques. Journal of Mechanics and Physics of Solids 43 (8), 1335–1348.

Zhao, H., Gary, G., 1996. On the use of SHPB techniques to determine the dynamic behaviour of materials in the range of small strains. International Journal of Solids and structures 33 (23), 3363–3375.

Zhao, H., Gary, G., 1997. A new method for the separation of waves. Application to the SHPB technique for an unlimited measuring duration. Journal of Mechanics and Physics of Solids 45, 1185–1202.

Zhao, H., Gary, G., 1998. Crushing behaviour of aluminium honeycombs under impact loading. International Journal of Impact Engineering 21 (10), 827–836.